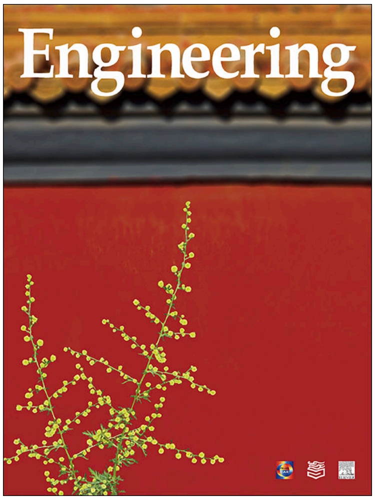

Article

Chemical Looping Steam Reforming of Methane under Mild Conditions via Non-Thermal Plasma

Zunrong Sheng, Donglong Fu, Tingting Yang, Xianhua Zhang, Zheyuan Ding, Chunlei Pei, Sai Chen, Zhi-Jian Zhao, Jinlong Gong

PII: S2095-8099(26)00001-9
DOI: https://doi.org/10.1016/j.eng.2026.01.001
Reference: ENG 2207

To appear in: *Engineering*

Received Date: 30 July 2024
Revised Date: 2 November 2025
Accepted Date: 3 January 2026

Please cite this article as: Z. Sheng, D. Fu, T. Yang, X. Zhang, Z. Ding, C. Pei, S. Chen, Z-J. Zhao, J. Gong, Chemical Looping Steam Reforming of Methane under Mild Conditions via Non-Thermal Plasma, *Engineering* (2026), doi: https://doi.org/10.1016/j.eng.2026.01.001

Research

Green Chemical Engineering—Article

Chemical Looping Steam Reforming of Methane under Mild Conditions via Non-Thermal Plasma

Zunrong Sheng [a,b,c,d], Donglong Fu [a,b,c], Tingting Yang [a,b,c,e], Xianhua Zhang [a,b,c,e], Zheyuan Ding [a,b,c], Chunlei Pei [a,b,c,f,g], Sai Chen [a,b,c], Zhi-Jian Zhao [a,b,c,f,g], Jinlong Gong [a,b,c,h,i,]*

[a] *Key Laboratory for Green Chemical Technology of Ministry of Education, School of Chemical Engineering and Technology, Tianjin University, Tianjin 300072, China*

[b] *Collaborative Innovation Center for Chemical Science and Engineering, Tianjin 300072, China*

[c] *International Joint Laboratory of Low-Carbon Chemical Engineering of Ministry of Education, Tianjin 300350, China*

[d] *School of Electrical Engineering, Dalian University of Technology, Dalian 116024, China*

[e] *Joint School of National University of Singapore and Tianjin University, International Campus of Tianjin University, Fuzhou 350207, China*

[f] *Haihe Laboratory of Sustainable Chemical Transformations, Tianjin 300192, China*

[g] *National Industry–Education Platform for Energy Storage, Tianjin University, Tianjin 300350, China*

[h] *State Key Laboratory of Synthetic Biology, Tianjin University, Tianjin 300072, China*

[i] *Tianjin Normal University, Tianjin 300387, China*

* Corresponding author.

E-mail address: jlgong@tju.edu.cn (J. Gong).

Abstract: The chemical looping steam reforming of methane (CL-SRM) holds immense potential for energy-efficient conversion of CH_4 into syngas and high-purity hydrogen. However, its large-scale implementation remains limited by high operating temperatures and substantial energy requirements. This paper describes a non-thermal plasma-mediated CL-SRM process based on CH_4/H_2O redox cycles over lanthanum-based perovskites under mild conditions. The developed process achieves efficient CH_4 activation at 600 °C, attaining 53.5% CH_4 conversion and 0.57 $mmol \cdot g^{-1}$ H_2 with 92% purity over $La_{0.5}Ce_{0.5}FeO_3$, while negligible conversion is observed under plasma-free conditions at the same furnace temperature. These performances surpass those observed under purely thermal conditions at 800 °C. Mechanistic insights reveal that plasma plays a crucial role in generating vibrationally excited CH_4^v species, thereby markedly lowering the reaction barrier for CH_4 activation. The plasma-mediated CL-SRM process delivers energy through voltage-induced electron transfer, offering the potential for adiabatic reactor designs that minimize energy consumption compared with conventional combustion-based systems suffering from heat transfer limitations.

Keywords: Non-thermal plasma; Redox chemistry; Steam reforming of methane

1. Introduction

Hydrogen, a versatile and clean energy carrier, has emerged as a key component in the transition toward a sustainable and environmentally conscious energy landscape. However, the production of H_2 remains a critical aspect of this paradigm shift.

Conventional steam reforming of methane accounts for nearly 50% of the global hydrogen production [1], yet the process requires energy-intensive separation of hydrogen from syngas [2,3]. The chemical looping steam reforming of methane (CL-SRM) technology [4–6] addresses this limitation by physically dividing the process into partial oxidation of methane (POM) and water splitting (WS), which yield syngas and high-purity hydrogen [7], respectively. Nevertheless, the high activation temperature required to cleave the C–H bond in methane and the limited lattice oxygen availability in oxygen carriers remain major barriers to practical implementation.

Extensive research has therefore focused on enhancing C–H bond activation and improving lattice oxygen availability. The activation of the C–H bond can be promoted by introducing metallic sites, such as Ni [8,9] and Fe [10], onto oxygen carriers, which facilitate the formation of active interface. Additionally, a reduced coordination number of metal cations in oxygen carriers has been shown to enhance C–H activation capacity [4]. In parallel, modification of the metal–oxygen bond has been employed to increase available active lattice oxygen species [9,11,12]. The creation of oxygen vacancies has been demonstrated to improve oxygen mobility from the bulk to the surface [13,14], while controlling oxygen concentration gradients can optimize the coordination of oxygen storage and release, for example, core–shell structured oxygen carriers have been developed to achieve high oxygen-carrying capacity and selective oxygen release [15–17]. However, despite these advances, such modification strategies still face practical challenges, including methane overactivation [18,19], poor cyclic stability, and structural irreversibility [9].

Non-thermal plasmas (NTPs) offer a facile and scalable approach for activating gas-phase molecules, thereby enabling thermodynamically unfavorable catalytic reactions over metal catalysts, such as POM [20], dry reforming [21–23], stream reforming [24–27], water–gas shift [28], CO_2 reduction [29], and ammonia synthesis [30]. Among various configurations, the dielectric barrier discharge (DBD) reactor is one of the most widely employed systems for NTP-assisted catalytic processes due to its cost-effectiveness, compact structure, and operational flexibility. In recent years, several studies have highlighted the role of DBD in facilitating the chemical looping of methane reforming under moderate temperatures [18,19,31]. For instance, Zheng et al. [18] reported a chemical looping process involving POM and air oxidation, in which CH_4 cracking and coke removal occur cyclically over a nickel-based metal oxide catalyst. Similarly, Ranganathan et al. [19] demonstrated methane dry reforming followed by WS at 150–400°C. However, these studies did not include temperature measurements during plasma operation [19], despite the potential for discharge-induced temperature increases [32,33]. Moreover, the reported CO selectivity during the POM step was only 3%–17% [18], and the H_2 yield during the WS step was merely 0.03 $mmol\cdot g^{-1}$ [19], both attributed to the weak transfer of lattice oxygen between CH_4 plasma species and the metal oxide. These findings underscore the critical need to simultaneously enhance C–H bond activation and optimize lattice oxygen availability in plasma-assisted CL—a domain that remains largely unexplored. Furthermore, the identification of key electron-induced plasma species and their interaction mechanisms with metal oxide surfaces remains elusive. Elucidating these processes is essential for understanding the synergistic interplay between plasma and oxygen carriers, which is pivotal for achieving efficient CL-SMR performance.

Here, we report that employing a packed-bed DBD reactor enables a reduction in operating temperature while simultaneously enhancing the availability of lattice oxygen in the CL-SRM process. Remarkable methane activation is achieved at a furnace temperature of 600 °C, yielding 53.5% CH_4 conversion and 0.57 $mmol\cdot g^{-1}$ H_2 with 92% purity over $La_{0.5}Ce_{0.5}FeO_3$. In contrast, negligible conversion is observed under plasma-free conditions at the same temperature. Notably, these results surpass those obtained under purely thermal activation at 800 °C. Mechanistic analysis highlights the crucial role of plasma in generating vibrationally excited CH_4^v species, which substantially lowers the reaction barrier for methane activation. Unlike conventional heat-driven processes, the plasma-mediated CL-SRM reaction is powered by electron energy, enabling the potential use of adiabatic reactor designs to minimize energy consumption compared with conventional combustion reactors limited by heat transfer resistance. This study offers a practical and energy-efficient route for methane activation under mild conditions using metal oxides.

2. Experimental section

2.1. DBD experimental apparatus

The schematic of the DBD system is shown in Fig. S1 in Appendix A. The oxygen carrier particles are packed within the discharge zone, serving as the dielectric medium. A sinusoidal high-voltage input from a plasma generator (CTP-2000K, Nanjing Suman Plasma Technology Co., Ltd., China) produces the DBD between a high-voltage electrode and a quartz-covered ground electrode. The discharge behavior is jointly regulated by the plasma generator and a voltage regulator equipped with adjustable voltage and frequency controls. The electrical signals are recorded using an oscilloscope

(MSO5104, 100 MHz, 8 GSa/s; Beijing Rigol Technology Co., Ltd., China) in conjunction with a high-voltage probe (P6015A, Tektronix Inc., USA) and a voltage probe. A sampling capacitor (10 nF) or resistor (50 Ω) is connected in series within a switchable circuit to capture the charge and current waveforms.

2.2. Preparation of oxygen carrier

State-of-the-art metal oxides, that is, $La_{0.5}Ce_{0.5}FeO_3$ (LaCeFe) and $LaFeO_3$ [11,34], were employed as oxygen carriers for both thermal catalytic and plasma-mediated CL-SRM in this study. Detailed characterization results are presented in Figs. S2 and S3 in Appendix A. $LaFeO_3$ and $La_{0.5}Ce_{0.5}FeO_3$ were synthesized via a sol–gel method [11] using $La(NO)_3·6H_2O$ (99.9%), $Ce(NO)_3·6H_2O$ (99.99%, used for $La_{0.5}Ce_{0.5}FeO_3$), and $Fe(NO)_3·9H_2O$ (98.5%), which are all purchased from Shanghai Macklin Biochemical Technology Co., Ltd. (China), in stoichiometric ratios according to the target composition. Citric acid (≥ 99.5%, Kermel Chemical Co., Ltd., China) and ethylene glycol (> 99%, Aladdin Co., Ltd., China) were added as dispersing agents at a molar ratio of 1.2:1.2:1 relative to the total metal ions. The gel precursor was prepared by evaporating the homogeneous solution with continuous stirring at 80 °C, followed by drying at 130 °C for 12 h. The resulting precursor was then calcined at 800 °C in air for 4 h to obtain $LaFeO_3$ or at 800 °C in 15 vol% CO_2/N_2 for $La_{0.5}Ce_{0.5}FeO_3$.

2.3. Temperature measurement

The temperature of the packed bed was monitored using an infrared (IR) thermal camera (348X+ Thermal Intelligence, Fotric Co., Ltd., USA) through an observation window (2 cm × 5 cm), as illustrated in Fig. S4 in Appendix A. The emissivity of the packed pellets was estimated to be 0.80 during both the POM and WS steps. Temperature control was achieved using an electrical furnace (BTF1200C, Anhui BEQ Equipment Technology Co., Ltd., China). The packed-bed temperature was governed by an overall energy balance, encompassing heat supplied by the external electrical furnace, heat generation from the DBD, heat consumption by endothermic reactions, and heat removal via gas flow. Considering the packed-bed temperature rise induced by DBD-generated heat, the furnace temperature was accordingly adjusted to maintain the target packed-bed temperature approximately.

2.4. Calculation of performance parameters

The process involved POM and WS (Fig. 1(a)) under continuous and isothermal redox conditions between 500 and 800 °C. The sequence consisted of the following steps: 6 min thermal POM, 15 min N_2 purging, 25 min WS, 15 min N_2 purging, 6 min plasma-assisted POM, 15 min N_2 purging, and 25 min WS (without plasma). The inlet gas flow and the corresponding temperature profile are schematically illustrated in Fig. S5 in Appendix A. Outlet gases were analyzed using an online gas chromatograph (Agilent 490 Micro GC, Agilent Technologies, Inc., USA) at 2 min sampling intervals after condensation through a cold trap. The CH_4 conversion (X_{CH_4}) and the selectivities of CO (S_{CO}), CO_2 (S_{CO_2}), C_2H_4 ($S_{C_2H_4}$), C_2H_6 ($S_{C_2H_6}$), and coke (S_{coke}), as well as the H_2/CO ratio ($R_{H_2/CO}$) and lattice oxygen consumption (X_{LO}) during the t min (t = 6) POM step, were calculated using Eqs. (1)–(8). The $F_{CH_4,in}$ is the inlet flow rate of CH_4. The m in Eqs. (8) – (10) is the weight of oxygen carrier. Outlet flow rates ($F_{M,out}$, M = CH_4, CO, CO_2, H_2, C_2H_4, C_2H_6) were determined by averaging the continuous data. The H_2 yield per cycle (Y_{H_2}), CO yield per cycle (Y_{CO}), and H_2 purity (Ψ_{H_2}) were calculated using Eqs. (9) –(11) during the t min (t = 25) WS step. The discharge power (P) in the plasma reaction was measured via voltage–charge Lissajous analysis and calculated using Eq. (12), where f, Q, and U represent the discharge frequency, accumulated charge, and applied voltage, respectively.

$$X_{CH_4} = \frac{F_{CH_4,in} - F_{CH_4,out}}{F_{CH_4,in}} \quad (1)$$

$$S_{CO} = \frac{F_{CO,out}}{F_{CH_4,in} - F_{CH_4,out}} \quad (2)$$

$$S_{CO_2} = \frac{F_{CO_2,out}}{F_{CH_4,in} - F_{CH_4,out}} \quad (3)$$

$$S_{C_2H_4} = \frac{2 \times F_{C_2H_4,out}}{F_{CH_4,in} - F_{CH_4,out}} \quad (4)$$

$$S_{C_2H_6} = \frac{2\times F_{C_2H_6,out}}{F_{CH_4,in} - F_{CH_4,out}} \quad (5)$$

$$S_{coke} = 1 - S_{CO} - S_{CO_2} - S_{C_2H_4} - S_{C_2H_6} \quad (6)$$

$$R_{H_2/CO} = \frac{F_{H_2,out}}{F_{CO,out}} \quad (7)$$

$$X_{LO} = \frac{(F_{CO,out} + F_{CO_2,out})\times t}{22.4\times m} \quad (8)$$

$$Y_{H_2} = \frac{F_{H_2,out}\times t}{22.4\times m} \quad (9)$$

$$Y_{CO} = \frac{F_{CO,out}\times t}{22.4\times m} \quad (10)$$

$$\Psi_{H_2} = \frac{Y_{H_2}}{Y_{H_2} + Y_{CO}} \quad (11)$$

$$P = f\oint Q\mathrm{d}U \quad (12)$$

3. Results and discussion

3.1. NTP-mediated CL-SRM

Time-resolved reaction data for the POM and WS steps are presented in Figs. S6 (LaCeFe case) and S7 ($LaFeO_3$ case) in Appendix A. These datasets include CH_4 conversion and the selectivities of H_2, CO, CO_2, and coke during the POM step, as well as the flow rates of H_2 and CO produced during the WS step. The DBD contributes Joule heating to both the reactor and the packed bed, resulting in an approximate 100 °C temperature rise when a 25 W discharge is applied during the plasma-mediated POM step. The corresponding temperature distribution, measured by the IR camera, is shown in Fig. S8 in Appendix A. As illustrated in Fig. 1(b), the introduction of plasma led to a pronounced enhancement in CH_4 conversion compared with pure thermal conditions. Specifically, CH_4 conversion increased from 21.4% at 605 °C (bed temperature) to 85.4% at 797 °C over LaCeFe, and from 15.9% to 71.6% over $LeFeO_3$. In contrast, negligible CH_4 conversion was observed below 700 °C for both oxides under thermal conditions. Remarkably, the plasma-assisted process achieved a CH_4 conversion of 53.5% at 704 °C, exceeding the value obtained at 800 °C under purely thermal operation.

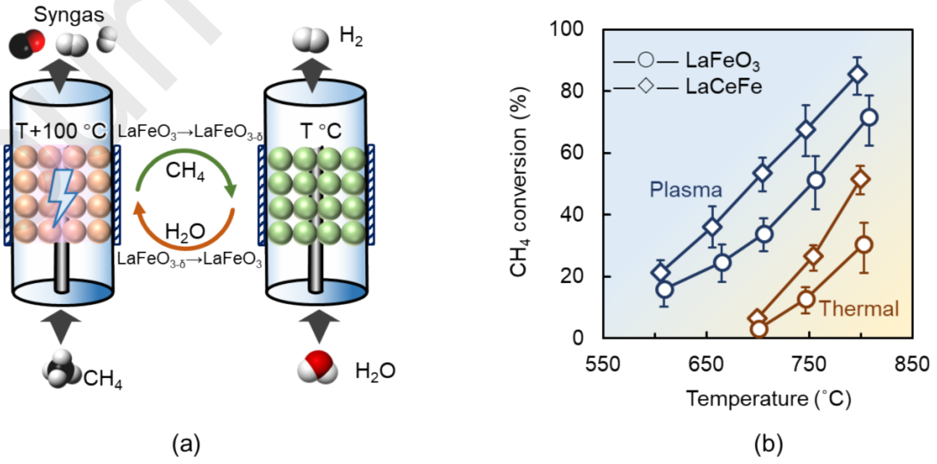

Fig. 1. Plasma-mediated CL-SRM. (a) Schematic illustration of the CL-SRM process, comprising a POM step and a WS step. (b) Average CH_4 conversion during 6 min of CL-SRM under purely thermal and plasma-mediated conditions over $LaFeO_3$ and LaCeFe as a function of bed temperature. The continuous flow rates of CH_4/N_2 (5/45 $cm^3\cdot min^{-1}$) and H_2O/N_2 (5/45 $cm^3\cdot min^{-1}$) were applied during the 6 min POM and 25 min

WS steps, respectively. The mass of the packed oxygen carrier was 1.5 g. The plasma power during the POM step was approximately 25 W. Note: the bed temperature (*T*) increased by approximately 100 °C when DBD was applied during the plasma-mediated POM step.

The lattice oxygen consumption during the POM cycle is summarized in Fig. 2(a). It increased from 0.22 to 0.87 mmol·g^{-1} for LaCeFe and from 0.13 to 0.60 mmol·g^{-1} for $LeFeO_3$ as the temperature rose from approximately 600 to 800 °C in plasma-mediated conditions, while negligible lattice oxygen conversion was observed below 700 °C for both LaCeFe and $LeFeO_3$ under thermal conditions. The H_2/CO ratio for LaCeFe remained around 2.2–2.3 at moderate temperatures of 600–700 °C. LaCeFe exhibited superior thermal performance compared with $LeFeO_3$ in terms of CH_4 and lattice oxygen conversion, attributable to its higher surface reaction activity and enhanced bulk oxygen mobility [11]. As shown in Figs. S6 and S7, the CO selectivity decreased slightly (by approximately 2%–3%) for the plasma-mediated POM cycle compared with pure thermal conditions for both oxygen carriers. This observation highlights the crucial role of plasma in promoting CH_4 activation for the selective production of syngas (H_2/CO).

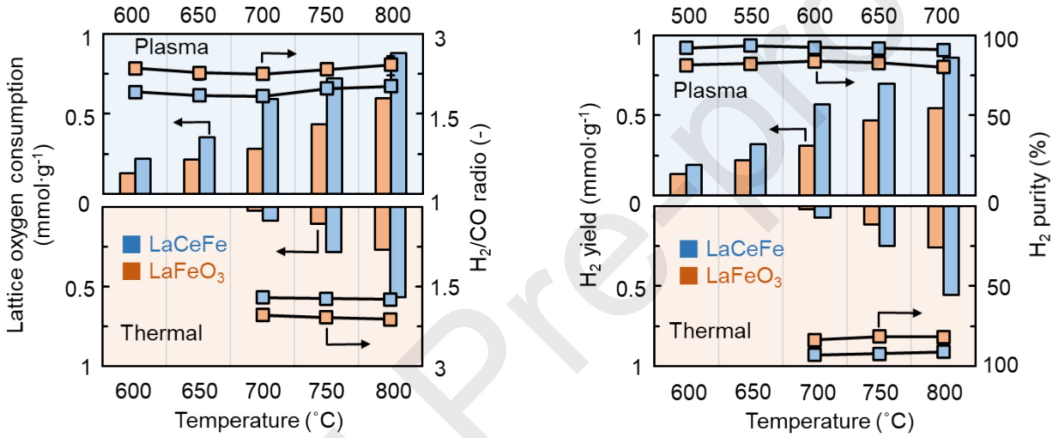

(a)

(b)

Fig. 2. Reaction performance of plasma-mediated CL-SRM over perovskite oxides. (a) Integral lattice oxygen consumption and H_2/CO ratio during the 6 min POM step. (b) Integral H_2 yield per cycle and H_2 purity during the WS step under purely thermal and plasma-mediated conditions over $LaFeO_3$ and LaCeFe as a function of temperature. Note: The furnace temperature was adjusted to maintain the same bed temperature for both plasma-mediated and purely thermal POM steps. Consequently, the WS step following plasma-mediated POM was conducted at a temperature approximately 100 °C lower than that following the thermal POM step.

WS was conducted following the POM step, either with plasma assistance (plasma-POM–WS) or without plasma (POM–WS). The bed temperature decreased once the plasma was turned off after the plasma-POM step. Plasma was not applied during the WS step due to the thermodynamically favorable nature of the reaction (Fig. S9 in Appendix A). As shown in Fig. 2(b), both metal oxides exhibited negligible H_2 yield at 600–700 °C under POM–WS conditions, producing 0.26 and 0.56 mmol·g^{-1} H_2 per cycle at 800 °C for $LeFeO_3$ and LaFeCe, respectively. In contrast, the plasma-POM–WS process achieved significantly higher H_2 yields, ranging from 0.19 to 0.86 mmol·g^{-1} across approximately 500–700 °C. The enhanced H_2 production in the plasma-POM–WS process is attributed to the efficient reduction of metal oxides by CH_4 in the plasma-mediated POM step, which consumes a greater number of lattice oxygen species and generates more oxygen vacancies, thereby intensifying the subsequent WS reaction. The H_2 purity in the LaCeFe system was approximately 91%–93%. As illustrated in Figs. S6 and S7, coke removal and CO generation occurred during the WS step between cycles. Furthermore, a durability test conducted at 600 °C using $LeFeO_3$ (Fig. S10 in Appendix A) demonstrated stable CH_4 conversion and H_2 yield over ten consecutive POM–WS cycles. Postreaction X-ray diffractometer (XRD; Bruker D8, Bruker AXS GmbH, Germany) and X-ray photoelectron spectroscopy (XPS; Thermo Fisher ESCALAB-Xi, Thermo Fisher Scientific, USA) analyses (Figs. S11 and S12 in Appendix A) confirmed the preservation of the perovskite crystal structure [34] and the chemical integrity of the oxygen carriers after repeated cycling.

3.2. Vibrationally excited CH_4^v-tuned POM reaction

The rate coefficients (k_e) for electron–molecule inelastic collision were calculated using BOLSIG+ with an appropriate cross-section set for CH_4 [35]. As shown in Fig. 3(a), the plasma reaction primarily promotes the formation of vibrationally excited CH_4^v. The k_e value for CH_4^v is several orders of magnitude higher than those for radical and ionized species within the 120–180 Td (1 Td = 10^{-21} V·m^2) range used in this study (see Table S1 in Appendix A for details). Radicals such as $\bullet CH_3$ and $\bullet CH_2$ contribute to the formation of C_2H_6 and C_2H_4, although the overall C_2 selectivity remains low at approximately 1.1% (Fig. S10). This finding is further supported by a control experiment using noncatalytic SiO_2 pellet-packed plasma, in which only minimal CH_4 conversion (< 1%) was observed (Fig. S13 in Appendix A).

To further elucidate the role of CH_4^v in the reaction, the generation rate of CH_4^v ($r_{CH_4^v}$) was adjusted based on electron–molecule collision theory and electrical diagnostics, as detailed in the Supplementary methods and Fig. S14 in Appendix A. $LaFeO_3$ was chosen as a representative catalyst due to its similar activation behavior to LaCeFe. The corresponding electrical, plasma, and reaction performance parameters are summarized in Table S1. As shown in Fig. 3(b), the CH_4 conversion rate (r_{CH_4}) increases linearly with $r_{CH_4^v}$, demonstrating that the plasma parameters effectively modulate the POM reaction, transforming it from a purely temperature-dependent process into one co-driven by both plasma and thermal effects. Furthermore, the generation rate of $\bullet CH_3$ radicals ($r_{\bullet CH_3}$) is significantly lower than the overall CH_4 conversion rate (Fig. S15 in Appendix A), indicating that dissociative species play a limited role in promoting CH_4 conversion.

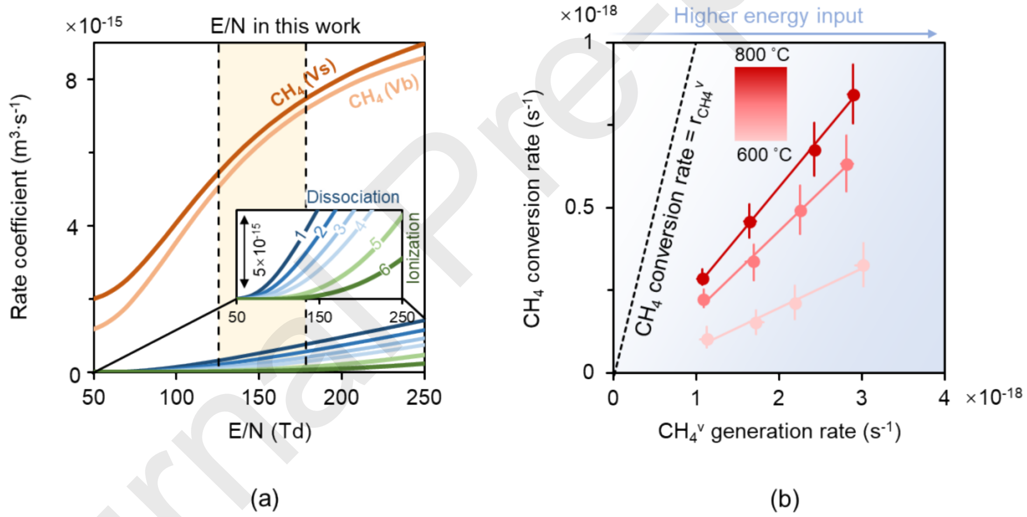

Fig. 3. DBD-induced vibrational excitation of methane for reaction enhancement. (a) Calculated rate coefficients as a function of reduced *E*/*N* (*E*: electric field; *N*: concentration of neutral particles; (1 Td = 10^{-21} V·m^2)) at CH_4/N_2 concentration ratio of 1:9, showing vibrationally excitation pathways (Vs: stretching vibration; Vb: bending vibration), dissociation pathways (1–4: $\bullet CH_3 + \bullet H$, $\bullet CH_2 + \bullet H$, $\bullet CH + H_2 + \bullet H$, and $C + 2H_2$, respectively), and ionization pathways (5 and 6: CH_4^+ and $CH_3^+ + \bullet H$, respectively). (b) Linear correlation between CH_4^v generation rate (i.e., generation rate of number of molecules of vibrationally excited methane) and CH_4 conversion rate (i.e., conversion rate of the number of molecules of methane) over $LaFeO_3$ under plasma conditions at 600–800 °C.

The density functional theory (DFT) study (described in the Supplementary methods) reveals that the energy barrier (E_a) for the dissociative chemisorption of ground-state CH_4^g (Figs. 4(a)–(c), selected from Fig. S16 in Appendix A) is 1.07 eV from the initial state to the transition state (TS), as shown in Fig. 4(d). This barrier is higher than that for bulk oxygen migration in $LaFeO_3$, which exhibits a potential energy of 0.5–0.7 eV [36,37] , respectively. These results suggest that CH_4 dissociative chemisorption represents the rate-limiting step with the highest energy barrier, consistent with previous studies [38]. The detailed DFT energy data are summarized in Table S2 (Appendix A). Furthermore, the elevated E_a primarily arises from the dissipation of vibrational energy associated with the symmetric stretching mode, rather than other vibrational modes (Fig. 4(e) and Table S3 in Appendix A). This indicates that the symmetric stretching vibration of CH_4 plays a dominant role in overcoming the C–H bond dissociation energy within the adiabatic molecule–surface interaction system. The symmetric stretching mode aligns more closely with the morphological evolution of the molecule during C–H bond cleavage over the surface than other vibrational modes. Similar morphological evolution has been confirmed in studies of bending vibrational CO_2-induced surface reaction enhancement [39,40].

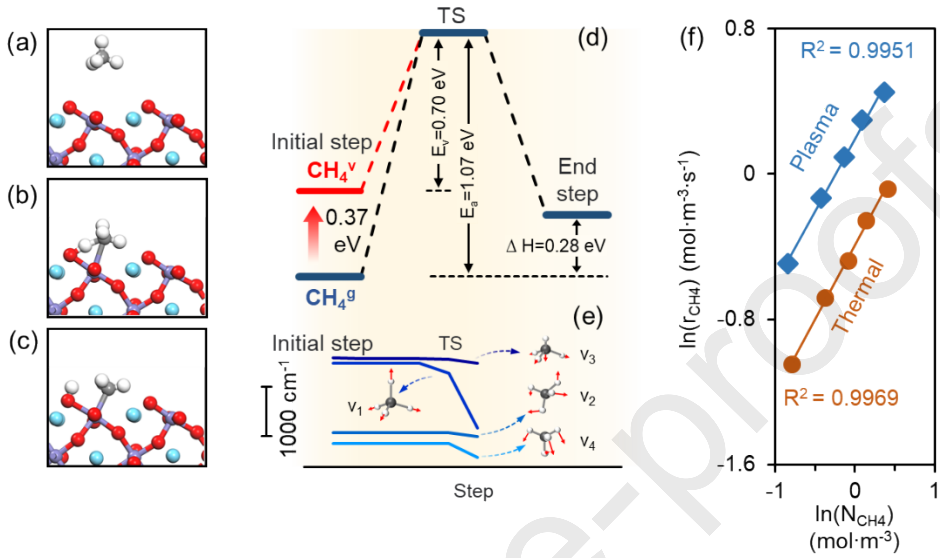

Fig. 4. CH_4^v-enhanced dissociative chemisorption over $LaFeO_3$(121). (a–c) Snapshots of the (a) initial, (b) TS, and (c) final configurations, where white, gray, red, blue, and purple spheres represent H, C, O, La, and Fe atoms, respectively. (d) Energy profiles for the dissociative chemisorption of ground-state methane (CH_4^g) and vibrationally excited methane (CH_4^v).ΔH is the reaction enthalpy for CH_4 chemisorption over $LaFeO_3$(121), and E_a and E_v denote the energy barriers for the dissociative chemisorption of ground-state CH_4^g and vibrationally excited CH_4^v, respectively. (e) Frequency variations of the four C–H vibrational modes from the initial step to the TS, where ν_1, ν_2, ν_3, and ν_4 correspond to symmetric stretching, torsional bending, antisymmetric stretching, and umbrella bending, respectively. (f) Influence of CH_4 concentration (N_{CH_4}) on the CH_4 conversion rate (r_{CH_4}) under thermal (orange circles) and plasma (blue diamonds) conditions at 720 °C with a plasma power of 12 W.

The kinetic analysis presented in Fig. 4(f) indicates that the reaction order (~0.8) remains unchanged upon plasma superposition. Details of the reaction order calculation are provided in the Supplementary methods, and the key parameters are summarized in Table S4 (Appendix A). This consistency suggests that the reaction mechanism, including the TS and the rate-determining step, remains largely unchanged for both CH_4^g and CH_4^v. The zero-point energy (ZPE) analysis (described in the Supplementary methods) shows that the intramolecular energy of methane in the vibrationally excited symmetric stretching mode is increased by 0.37 eV relative to the vibrational ground state. We infer that this excited state is intrinsically less stable and more prone to vibrational energy dissipation, thereby facilitating C–H bond cleavage. As a result, the reaction barrier decreases from 1.07 to 0.70 eV (Fig. 4(d)). This mode-selective enhancement of the C–H vibrational level in the symmetric stretching mode is realized under plasma conditions, where vibrationally excited methane (CH_4^v in stretching vibration) is the dominant species (Fig. 3(a)). Collectively, these findings demonstrate that CH_4^v, generated through low-energy electron collisions, provides the principal driving force for the observed reaction enhancement.

3.3. Enhancement of oxygen species accessibility

The *in-situ* plasma diffuse reflectance infrared Fourier-transform spectroscopy (DRIFTS) study (experimental details provided in the Supplementary methods and Fig. S17 in Appendix A) reveals that no surface dehydrogenation products are from thermal CH_4, as shown in spectrum (i) of Fig. 5(a). In contrast, hydrocarbon fragments [41] at 1425 cm^{-1} and CH_x (x = 1–3) species [9,42–44] in the 2850–3000 cm^{-1} range appear in spectra (ii) under CH_4 plasma, indicating that dissociative chemisorption is significantly enhanced during plasma-assisted reaction. The surface hydroxyl (OH) group, a key intermediate in steam-involved chemical looping [45], acts as a surface-adsorbed oxygen species that participates in redox reactions with CH_4-derived intermediates [46,47]. A weak but distinct negative peak at 3655 cm^{-1} is observed in the thermal reaction (spectrum (i)), corresponding to the consumption of OH species. This peak becomes much stronger under plasma conditions (spectra (ii)), suggesting more extensive OH consumption. These results indicate that surface-adsorbed oxygen species react with CH_4-derived intermediates to generate CO* [46–48] (2168 cm^{-1}), formate [41,49] (1576 and 1377 cm^{-1}), and carbonate species [50] (1681 and 1710 cm^{-1}), ultimately producing CO, as confirmed by the quadrupole mass spectrometer (MS) signal in Fig. 5(b). Based on these observations, we propose that the redox between CH_4 and $LaFeO_3$ proceeds via a Langmuir–Hinshelwood mechanism, where CH_4 plasma enabling strong accessibility to surface-adsorbed oxygen (O*) species.

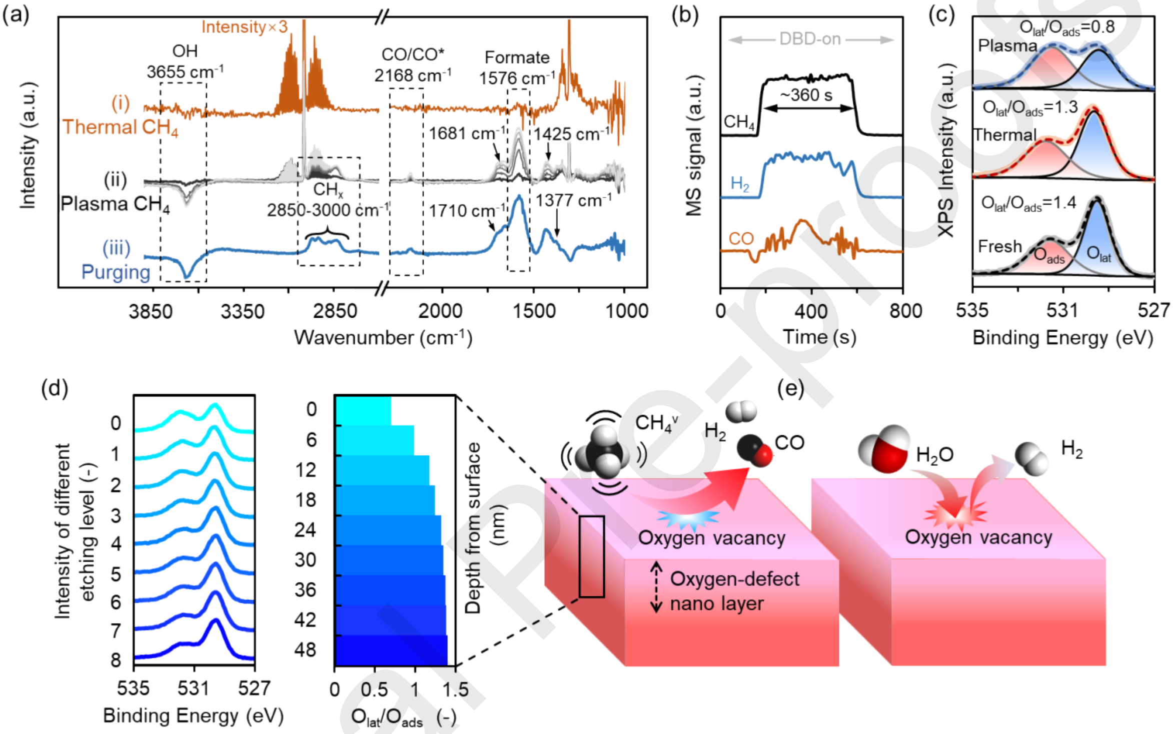

Fig. 5. Plasma-enhanced accessibility of oxygen species. (a) *In-situ* plasma DRIFTS spectra of $LaFeO_3$ under the following conditions: (i) CH_4 treatment with plasma off, (ii) CH_4 treatment with plasma on (sampling interval: 60 s), and (iii) subsequent N_2 purging. (b) Time-resolved MS profiles of gaseous products obtained from the *in-situ* plasma DRIFTS experiment. (c) XPS analysis of lattice oxygen behavior in fresh $LaFeO_3$ and samples treated under CH_4 plasma and thermal CH_4 conditions. O_{lat}: lattice oxygen; O_{ads}: adsorbed oxygen. (d) O 1s spectra and lattice-to-adsorbed oxygen area ratio (O_{lat}/O_{ads}) as a function of depth from the surface for CH_4 plasma-treated $LaFeO_3$. (e) Schematic illustration of oxygen-deficient nanolayer formation and the potential reaction pathway for the WS step facilitated by oxygen vacancies.

The deoxygenation behavior in the bulk phase was investigated using XPS (described in the Supplementary methods), as shown in Fig. 5(c). The sample treated with thermal CH_4 exhibited a similar lattice-to-adsorbed oxygen area ratio [51] ($O_{lat}/O_{ads} = 1.3$) to that of the fresh sample ($O_{lat}/O_{ads} = 1.4$), indicating negligible lattice oxygen consumption due to limited surface reactions, consistent with the *in-situ* plasma DRIFTS observations. In contrast, the CH_4 plasma-treated sample showed a notable decrease in the O_{lat}/O_{ads} ratio from 1.4 to 0.8 (Fig. 5(c)), accompanied by a shift of the Fe 2p peak [52] toward lower binding energy (Fig. S18 in Appendix A). These findings confirm that CH_4 plasma promotes surface redox reactions, consuming lattice oxygen in $LaFeO_3$ and generating oxygen-deficient $LaFeO_{3-\delta}$ with oxygen vacancies. Furthermore, the chemical potential gradient of lattice oxygen induced by CH_4 plasma was evidenced by depth profiling analysis (Supplementary methods and Fig. S19 in Appendix A). As shown in Fig. 5(d), the O_{lat}/O_{ads} ratio increases gradually from the surface to a depth of 20–30 nm, illustrating that CH_4 plasma preferentially depletes surface lattice oxygen to form a nanoscale oxygen-deficient layer, as illustrated schematically in Fig. 5(e). These surface oxygen vacancies serve as reaction sites for H_2O dissociation and H_2 generation during the subsequent WS step [53]. Meanwhile, the valence state and relative content of lanthanum species remained unchanged during the surface redox process (Fig. S18). Collectively, these results demonstrate that plasma activation markedly enhances lattice oxygen accessibility in metal oxides during CH_4 activation.

3.4. Energy comparison between the plasma-mediated endothermic reaction and other processes

Energy analysis was performed based on the reaction conditions employed in this study, comparing plasma-mediated and purely thermal processes with comparable reaction performance (Supplementary methods and Table S5 in Appendix A). As shown in Fig. 6(a), the plasma reactor operating at a furnace temperature of 600 °C required 26.3 kJ of sensible heat, whereas the pure thermal process demanded 35.4 kJ at 800 °C (Fig. 6(b)). The reduced sensible heat requirement not only enhances the start-up and shut-down efficiency of the system but also lowers operational costs and mitigates the risks associated with high-temperature operation. Furthermore, a comparison of the reaction data at 600 °C for the plasma-mediated (Fig. 6(a)) and pure thermal processes (Fig. 6(c)) reveals that the energy necessary to drive the POM reaction can be supplied entirely by plasma. Specifically, no CH_4 conversion was detected at 600 °C under pure thermal conditions (Fig. 6(c)), whereas the introduction of plasma achieved a 53% CH_4 conversion (Fig. 6(a)). These findings suggest the feasibility of employing an adiabatic reactor configuration for the plasma-mediated process, wherein the required energy is delivered directly through an alternating current (AC) voltage-driven discharge rather than external heating.

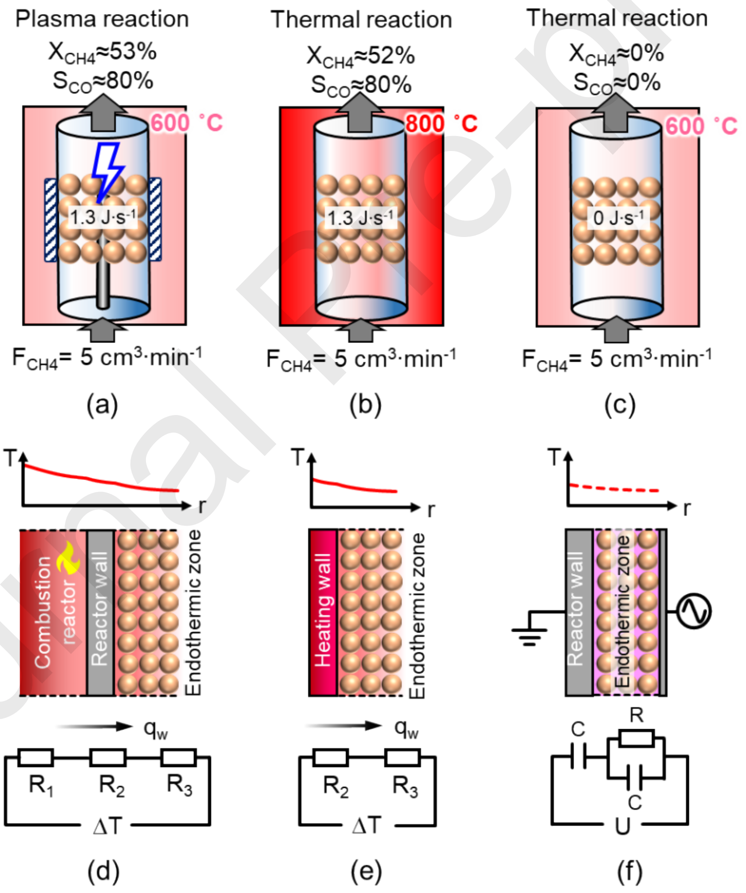

Fig. 6. Energy comparison of the plasma-mediated endothermic reaction with other processes. (a–c) Schematic illustrations of endothermic behavior and energy supply for: (a) plasma-mediated reaction at 600 °C, (b) thermal reaction at 800 °C, and (c) thermal reaction at 600 °C. (d–f) Schematic representations of heat/energy transfer models, including radial temperature profiles (top) and equivalent thermal resistance circuits (bottom) or equivalent alternating current (AC)-driven DBD circuits (bottom): (d) conventional fired reactor [54], (e) electrically resistance-heated reactor [1], and (f) plasma reactor. R, q_w, ΔT, C, U, and r denote thermal/electrical resistance, inward heat flux, temperature gradient, equivalent capacitance, applied AC voltage, and radial position, respectively.

Exergy analysis was performed to evaluate the heat conduction mechanism from various external energy sources into the endothermic reactor, with detailed parameters summarized in Table S6 (Appendix A). The conventional fired reactor operates under an “endothermic zone + exothermic reactor” configuration, as schematically illustrated in Fig. 6(d). In this system, the combustion (exothermic) reactor generates a high temperature gradient ($\Delta T > 300$ °C) through fuel combustion, providing an inward heat flux of 390 $\mathrm{W \cdot cm^{-2}}$ to sustain a 2452 $\mathrm{J \cdot s^{-1}}$ endothermic reaction. This substantial heat flux arises from the thermal-resistance-induced temperature profile across the reactor wall [54]. Wismann et al. [1] reported that electric resistance heating, which operates under an “heating wall + endothermic zone” mode, delivers a lower equivalent inward heat flux of 180 $\mathrm{W \cdot cm^{-2}}$ for a 260 $\mathrm{J \cdot s^{-1}}$ endothermic process (Fig. 6(e)). This improvement results from a reduced temperature gradient and decreased thermal resistance owing to a uniformly heated wall closer to the endothermic zone. In contrast, the plasma reactor significantly optimizes the energy transfer pathway, as plasma energy is supplied directly through voltage-driven discharge rather than by conventional heat conduction. As depicted in Fig. 6(f), the plasma reactor delivers energy directly into the endothermic zone across the reactor wall via AC-voltage excitation, enabling adiabatic operation where external heat supply becomes unnecessary. Consequently, a mild equivalent energy flux of 4.0 $\mathrm{W \cdot cm^{-2}}$ is sufficient to sustain an endothermic reaction rate of 1.4 $\mathrm{J \cdot s^{-1}}$, demonstrating markedly higher energy-transfer efficiency than both the fired and electric-resistance reactor configurations.

The maximum energy efficiency of plasma-enhanced hydrogen production was estimated at 25.5% for the LaCeFe system, calculated based on the lower heating value of H_2 (calculation details in Supplementary methods). As shown in Fig. S20 in Appendix A, the H_2 yield per cycle increases with temperature, rising from 0.59 to 1.50 mmol per cycle for $LaFeO_3$ and from 0.82 to 1.91 mmol per cycle for LaCeFe. Correspondingly, the energy efficiency increases from 7.9% to 20.1% and from 11.0% to 25.5% for the respective materials. This improvement is attributed to enhanced surface activity of the oxygen carriers, which promotes synergistic interactions between the plasma and the catalytic surface. Notably, a slight decline in efficiency for LaCeFe between 700 and 800 °C is attributed to its intrinsically high thermal activity, which diminishes the relative contribution of plasma-induced enhancement under these conditions.

4. Conclusions

In summary, this study demonstrates that NTP enables methane reforming at mild temperatures through a chemical looping process over perovskite oxides. The plasma-mediated system achieved 53.5% CH_4 conversion and an H_2 yield of 0.57 $\mathrm{mmol \cdot g^{-1}}$ with 92% purity at 600 °C, far exceeding the performance of the pure thermal process under identical conditions and even surpassing that at 800 °C. This remarkable enhancement arises from the lowered reaction barrier for CH_4 activation, driven by vibrationally excited CH_4^v generated in the plasma. The developed process utilizes electron energy rather than thermal energy to drive CH_4 activation, enabling a potentially adiabatic reactor design that can significantly reduce overall energy consumption. This study presents an effective plasma-mediated external-field-enhanced method for inert molecule activation over metal oxide, and introduces an innovative electrified approach to supply energy for strong endothermic reactions, thereby reducing energy requirements.

Acknowledgments

This work was supported by the National Key Research and Development Program (2023YFA1507800 and 2021YFA1501303), the National Natural Science Foundation of China (22208239, 22121004, and U20B6002), the China Postdoctoral Science Foundation (2021TQ0240), the Haihe Laboratory of Sustainable Chemical Transformations (CYZC202107), and the Program of Introducing Talents of Discipline to Universities, and the XPLORER PRIZE.

Appendix A. Supplementary data

Supplementary data to this article can be found online.

References

[1] Wismann ST, Engbæk JS, Vendelbo SB, Bendixen FB, Eriksen WL, Aasberg-Petersen K, et al. Electrified methane reforming: a compact approach to greener industrial hydrogen production. Science 2019;364(6442):756–9.

[2] Ben-Mansour R, Azazul Haque MD, Harale A, Paglieri SN, Alrashed FS, Raghib Shakeel M, et al. Comprehensive parametric investigation of methane reforming and hydrogen separation using a CFD model. Energy Convers Manage 2021;249:114838.

[3] Song C, Liu Q, Ji N, Kansha Y, Tsutsumi A. Optimization of steam methane reforming coupled with pressure swing adsorption hydrogen production process by heat integration. Appl Energy 2015;154:392–401.

[4] Liu K, Pan C, Kuhn A, Nievergelt AP, Fantner GE, Milenkovic O, et al. Detecting topological variations of DNA at single-molecule level. Nat Commun 2019;10:3.

[5] Wang W, Chen S, Pei C, Luo R, Sun J, Song H, et al. Tandem propane dehydrogenation and surface oxidation catalysts for selective propylene synthesis. Science 2023;381(6660):886–90.

[6] Metcalfe IS, Ray B, Dejoie C, Hu W, de Leeuwe C, Dueso C, et al. Overcoming chemical equilibrium limitations using a thermodynamically reversible chemical reactor. Nat Chem 2019;11(7):638–43.

[7] Muhich CL, Evanko BW, Weston KC, Lichty P, Liang X, Martinek J, et al. Efficient generation of H_2 by splitting water with an isothermal redox cycle. Science 2013;341(6145):540–2.

[8] Huang J, Liu W, Yang Y, Liu B. High-performance Ni–Fe redox catalysts for selective CH_4 to syngas conversion via chemical looping. ACS Catal 2018;8(3):1748–56.

[9] Chen S, Zeng L, Tian H, Li X, Gong J. Enhanced lattice oxygen reactivity over Ni-modified WO_3-based redox catalysts for chemical looping partial oxidation of methane. ACS Catal 2017;7(5):3548–59.

[10] Kang Y, Han Y, Tian M, Huang C, Wang C, Lin J, et al. Promoted methane conversion to syngas over Fe-based garnets via chemical looping. Appl Catal B 2020;278:119305.

[11] Zhang X, Pei C, Chang X, Chen S, Liu R, Zhao ZJ, et al. FeO_6 octahedral distortion activates lattice oxygen in perovskite ferrite for methane partial oxidation coupled with CO_2 splitting. J Am Chem Soc 2020;142(26):11540–9.

[12] Liu R, Pei C, Zhang X, Chen S, Li H, Zeng L, et al. Chemical looping partial oxidation over $FeWO_x/SiO_2$ catalysts. Chin J Catal 2020;41(7):1140–51.

[13] Chang H, Bjørgum E, Mihai O, Yang J, Lein HL, Grande T, et al. Effects of oxygen mobility in La–Fe-based perovskites on the catalytic activity and selectivity of methane oxidation. ACS Catal 2020;10(6):3707–19.

[14] Kang Y, Tian M, Huang C, Lin J, Hou B, Pan X, et al. Improving syngas selectivity of Fe_2O_3/Al_2O_3 with yttrium modification in chemical looping methane conversion. ACS Catal 2019;9(9):8373–82.

[15] Zhang X, Liu R, Liu T, Pei C, Gong J. Redox catalysts for chemical looping methane conversion. Trends Chem 2023;5(7):512–25.

[16] Ma S, Chen S, Zhu M, Zhao Z, Hu J, Wu M, et al. Enhanced sintering resistance of Fe_2O_3/CeO_2 oxygen carrier for chemical looping hydrogen generation using core–shell structure. Int J Hydrogen Energy 2019;44(13):6491–504.

[17] Neal L, Shafiefarhood A, Li F. Effect of core and shell compositions on $MeO_x@La_ySr_{1-y}FeO_3$ core–shell redox catalysts for chemical looping reforming of methane. Appl Energy 2015;157:391–8.

[18] Zheng Y, Marek EJ, Scott SA. H_2 production from a plasma-assisted chemical looping system from the partial oxidation of CH_4 at mild temperatures. Chem Eng J 2020;379:122197.

[19] Ranganathan RV, Jony B, Fondriest SM, Liu Z, Wang R, Uddi M. Plasma-catalysis chemical looping CH_4 reforming with water splitting using ceria supported Ni based La-perovskite nano-catalyst. J CO_2 Util 2019;32:11–20.

[20] Gibson EK, Stere CE, Curran-McAteer B, Jones W, Cibin G, Gianolio D, et al. Probing the role of a non‐thermal plasma (NTP) in the hybrid NTP catalytic oxidation of methane. Angew Chem Int Ed 2017;56(32):9351–5.

[21] Winter LR, Chen JG. Challenges and opportunities in plasma-activated reactions of CO_2 with light alkanes. J Energy Chem 2023;84:424–7.

[22] Loenders B, Michiels R, Bogaerts A. Is a catalyst always beneficial in plasma catalysis? Insights from the many physical and chemical interactions. J Energy Chem 2023;85:501–33.

[23] Wang L, Yi Y, Wu C, Guo H, Tu X. One-step reforming of CO_2 and CH_4 into high‐value liquid chemicals and fuels at room temperature by plasma-driven catalysis. Angew Chem 2017;129(44):13867–71.

[24] Geng F, Haribal VP, Hicks JC. Non-thermal plasma-assisted steam methane reforming for electrically-driven hydrogen production. Appl Catal A 2022;647:118903.

[25] Bajpai A, Mehta S, Joshi K, Kumar S. Hydrogen from catalytic non-thermal plasma-assisted steam methane reforming reaction. Int J Hydrogen Energy 2023;48(63):24328–41.

[26] Zhu X, Liu X, Lian HY, Liu JL, Li XS. Plasma catalytic steam methane reforming for distributed hydrogen production. Catal Today 2019;337:69–75.

[27] Hrabovsky M, Hlina M, Kopecky V, Maslani A, Krenek P, Serov A, et al. Steam plasma methane reforming for hydrogen production. Plasma Chem Plasma Process 2018;38(4):743–58.

[28] Stere CE, Anderson JA, Chansai S, Delgado JJ, Goguet A, Graham WG, et al. Non-thermal plasma activation of gold-based catalysts for low-temperature water–gas shift catalysis. Angew Chem Int Ed 2017;56(20):5579–83.

[29] Mistry H, Varela AS, Bonifacio CS, Zegkinoglou I, Sinev I, Choi YW, et al. Highly selective plasma-activated copper catalysts for carbon dioxide reduction to ethylene. Nat Commun 2016;7:12123.

[30] Mehta P, Barboun P, Herrera FA, Kim J, Rumbach P, Go DB, et al. Overcoming ammonia synthesis scaling relations with plasma-enabled catalysis. Nat Catal 2018;1(4):269–75.

[31] Zheng Y, Grant R, Hu W, Marek E, Scott SA. H_2 production from partial oxidation of CH_4 by Fe_2O_3-supported Ni-based catalysts in a plasma-assisted packed bed reactor. Proc Combust Inst 2019;37(4):5481–8.

[32] Nozaki T, Okazaki K. Non-thermal plasma catalysis of methane: principles, energy efficiency, and applications. Catal Today 2013;211:29–38.

[33] Sheng Z, Watanabe Y, Kim HH, Yao S, Nozaki T. Plasma-enabled mode-selective activation of CH_4 for dry reforming: first touch on the kinetic analysis. Chem Eng J 2020;399:125751.

[34] Xing Y, Fan Y, Yan Z, Zhao B, Huang Y, Pan W. Core–shell LaOCl/$LaFeO_3$ nanofibers with matched impedance for high-efficiency electromagnetic wave absorption. Sci China Mater 2023;66(4):1587–96.

[35] Morgan WL. A critical evaluation of low-energy electron impact cross sections for plasma processing modeling. II: Cl_4, SiH_4, and CH_4. Plasma Chem Plasma Process 1992;12(4):477–93.

[36] Taylor FH, Buckeridge J, Catlow CRA. Defects and oxide ion migration in the solid oxide fuel cell cathode material $LaFeO_3$. Chem Mater 2016;28(22):8210–20.

[37] Jones A, Islam MS. Atomic-scale insight into $LaFeO_3$ perovskite: defect nanoclusters and ion migration. J Phys Chem C 2008;112(12):4455–62.

[38] Yang J, Bjørgum E, Chang H, Zhu KK, Sui ZJ, Zhou XG, et al. On the ensemble requirement of fully selective chemical looping methane partial oxidation over La–Fe-based perovskites. Appl Catal B 2022;301:120788.

[39] Kim DY, Ham H, Chen X, Liu S, Xu H, Lu B, et al. Cooperative catalysis of vibrationally excited CO_2 and alloy catalyst breaks the thermodynamic equilibrium limitation. J Am Chem Soc 2022;144(31):14140–9.

[40] Quan J, Muttaqien F, Kondo T, Kozarashi T, Mogi T, Imabayashi T, et al. Vibration-driven reaction of CO_2 on Cu surfaces via Eley–Rideal-type mechanism. Nat Chem 2019;11(8):722–9.

[41] Alharbi AA, Sackmann A, Weimar U, Bârsan N. Acetylene- and ethylene-sensing mechanism for $LaFeO_3$-based gas sensors: operando insights. J Phys Chem C 2020;124(13):7317–26.

[42] Shao S, Zhang H, Xiao R, Li X, Cai Y. Catalytic conversion of biomass-derivates by *in situ* DRIFTS: evolution of coke. J Anal Appl Pyrolysis 2017;127:258–68.

[43] Guo J, Hou Z, Gao J, Zheng X. DRIFTS study on adsorption and activation of CH_4 and CO_2 over Ni/SiO_2 catalyst with various Ni particle sizes. Chin J Catal 2007;28(1):22–6.

[44] Kuhn JN, Ozkan US. Surface properties of Sr- and Co-doped $LaFeO_3$. J Catal 2008;253(1):200–11.

[45] He F, Li X, Zhao K, Huang Z, Wei G, Li H. The use of $La_{1-x}Sr_xFeO_3$ perovskite-type oxides as oxygen carriers in chemical-looping reforming of methane. Fuel 2013;108:465–73.

[46] Kim J, Kim YJ, Ferree M, Gunduz S, Co AC, Kim M, et al. *In-situ* exsolution of bimetallic CoFe nanoparticles on (La,Sr)FeO_3 perovskite: its effect on electrocatalytic oxidative coupling of methane. Appl Catal B 2023;321:122026.

[47] Wang Y, Hu P, Yang J, Zhu YA, Chen D. C–H bond activation in light alkanes: a theoretical perspective. Chem Soc Rev 2021;50(7):4299–358.

[48] Amrillah T, Supandi AR, Puspasari V, Hermawan A, Seh ZW. MXene-based photocatalysts and electrocatalysts for CO_2 conversion to chemicals. Trans Tianjin Univ 2022;28(4):307–22.

[49] Alharbi A, Junker B, Alduraibi M, Algarni A, Weimar U, Bârsan N. The role of different lanthanoid and transition metals in perovskite gas sensors. Sensors 2021;21(24):8462.

[50] Sheng Z, Kim HH, Yao S, Nozaki T. Plasma-chemical promotion of catalysis for CH_4 dry reforming: unveiling plasma-enabled reaction mechanisms. Phys Chem Chem Phys 2020;22(34):19349–58.

[51] Donat F, Müller CR. CO_2-free conversion of CH_4 to syngas using chemical looping. Appl Catal B 2020;278:119328.

[52] Sun X, Zhu L, Zhao W, Li F, Chen X. Ni–Fe bimetallic hexaaluminate for efficient reduction of O_2-containing CO_2 via chemical looping. Chem Eng J 2022;441:136071.

[53] Zeng L, Cheng Z, Fan JA, Fan LS, Gong J. Metal oxide redox chemistry for chemical looping processes. Nat Rev Chem 2018;2(11):349–64.

[54] Ngo SI, Lim YI, Kim W, Seo DJ, Yoon WL. Computational fluid dynamics and experimental validation of a compact steam methane reformer for hydrogen production from natural gas. Appl Energy 2019;236:340–53.

Declaration of interests

☒ The authors declare that they have no known competing financial interests or personal relationships that could have appeared to influence the work reported in this paper.

☐ The author is an Editorial Board Member/Editor-in-Chief/Associate Editor/Guest Editor for *[Journal name]* and was not involved in the editorial review or the decision to publish this article.

☐ The authors declare the following financial interests/personal relationships which may be considered as potential competing interests: